Time-resolved photoluminescence study of excitons in α-PTCDA as a function of temperature

A. Yu. Kobitski,* R. Scholz,† and D. R. T. Zahn
Institut für Physik, Technische Universität, D-09107 Chemnitz, Germany

H. P. Wagner
Department of Physics, University of Cincinnati, Ohio 45221, USA

(Received 17 January 2003; revised manuscript received 19 May 2003; published 1 October 2003)

In the present work, we analyze the radiative and nonradiative recombination channels in α-PTCDA (3,4,9,10-perylene tetracarboxylic dianhydride) by applying time-resolved photoluminescence (PL) techniques in the 50 ns range between temperatures of $T=10$ K and $T=300$ K. The obtained PL spectra are decomposed into exponentially decaying components which can be assigned to different types of excitons, including Frenkel excitons, three types of self-trapped excitons, and two different high-energy PL satellites. From the temperature dependence of the PL spectra, we gain some insight into the influence of nonradiative processes on the decay time of the different PL bands. At room temperature, PL from Frenkel excitons and oppositely charged ionic pairs is quenched due to nonradiative recombination. In contrast to this behavior, the decay of a PL band assigned to excimers shows only a weak temperature dependence, so that it becomes the dominating radiative recombination mechanism at temperatures above $T=200$ K.

DOI: 10.1103/PhysRevB.68.155201 PACS number(s): 71.35.Aa, 78.20.Bh, 78.47.+p

I. INTRODUCTION

Even though the optical properties and the photoluminescence (PL) mechanisms of organic semiconductors are crucial for optoelectronic device applications, present understanding of their microscopic foundation is still rather limited. Due to the progress in purification and growth techniques, reproducible optical absorption spectra have been obtained for a variety of reference systems, including polyacenes, thiophenes, and perylene derivatives. Polycrystalline films of the planar molecule 3,4,9,10-perylene tetracarboxylic dianhydride (PTCDA) were used as an interesting model system for studying the influence of intermolecular interactions on the structural, optical, and electronic properties.[1,2] The linear optical properties were investigated with a large variety of theoretical approaches, including exciton models adapted from inorganic semiconductors,[1] Frenkel excitons,[3] and schemes allowing for both Frenkel and charge-transfer (CT) excitons.[4,5] Compared to the spectra of single molecules in weakly interacting surroundings,[6] the absorption spectra in the solid phase are strongly redshifted, so that their analysis requires microscopic models for the reduction of the optical transition energy.

An interesting alternative for the determination of the microscopic parameters of the various kinds of excitons are time-resolved PL spectra. Early measurements of the PL decay time in PTCDA thin films[7] were interpreted with CT excitons,[8] and at higher temperature, the much faster decay was found to be nonexponential and energy dependent,[9] with a rather low PL efficiency at room temperature.[10] For ultrathin amorphous PTCDA films,[11] the PL decay approaches the molecular limit known from dissolved monomers,[8,11] and in a different perylene derivative, MePTCDI, the temporal dynamics of the PL spectra were assigned to an excimer state.[12]

In the present work, we extend our previous low-temperature and room-temperature investigations[13,14] to the temperature dependence of time-resolved PL measured on single crystals of α-PTCDA. Based on a numerical data analysis, we can extract different contributions to the PL spectra. The assignment of the observed PL bands is based on microscopic calculations of Frenkel[15,16] and self-trapped excitons (STE's), like excimers and CT excitons,[15,17] suggesting that all the PL mechanisms discussed previously can occur in the same material.

In Sec. II, we discuss the experimental setup and present the time-integrated PL at different temperatures. Based on previous model calculations,[16–18] we propose in Sec. III microscopic assignments for the observed PL bands. For each of these PL channels, the shape results from a vibronic progression over different levels of an effective vibrational mode. As the interpolation of the line shapes between different temperatures and the numerical fitting technique are rather involved, we dedicate Sec. IV to the various quantitative details. In Sec. V, we compare the measured temperature-dependent PL decay rates and relative intensities of the different bands to a kinetic model involving activated nonradiative recombination and energetic barriers for the formation of the self-trapped excitons. The paper is concluded in Sec. VI.

II. EXPERIMENT

The α-PTCDA crystals used in the present investigation were grown by double sublimation in high vacuum (2×10^{-6} mbar). For the time-resolved PL measurements these single crystals were excited with a pulsed dye laser synchronously pumped by a mode-locked Ar^+ ion laser, resulting in 20 ps pulses at an energy of 2.19 eV (565 nm) focused to a spot of about 250 μm on the sample. As the repetition rate of 80 MHz defined by the cavity length of the ion laser exceeds the decay rate of the slowest PL components, it was reduced to 4 MHz using a cavity dumper. The time-resolved PL was analyzed using a CROMEX 250IS imaging spectrograph and detected by a Hamamatsu C4334 Streakscope with a time

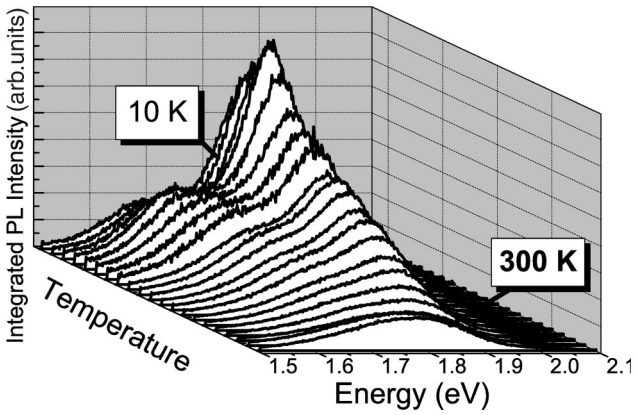

FIG. 1. Time-integrated PL spectra (delay -5 ns to 45 ns) measured on a single crystal of α-PTCDA, at different temperatures $T=10$, 15, 20, 30, 40, 60, 80, 100, 125, 150, 160, 170, 180, 190, 200, 210, 225, 240, 260, 280, and 300 K.

resolution better than 50 ps. In order to protect the streakscope against stray light from the laser, a filter with a cutoff at 590 nm (2.10 eV) was used. In the range 1.5–2.1 eV investigated in the present work, the flatness of the spectral response of the entire measuring system was checked with blackbody radiation from a tungsten lamp with known emission spectrum, and therefore no spectral correction was applied to the subsequent PL measurements. For the temperature-dependent investigations ($T=10$–300 K), a closed-cycle He cryostat CTI-Cryogenics was used. As the intensity of the PL was proportional to the laser fluence, without any variations in the spectral shape, we exclude exciton-exciton interactions as a relevant decay route.

The transient PL data measured over a temperature range of 10–300 K were recorded from about 5 ns before the laser pulse to 45 ns after the excitation. A set of PL spectra at different temperatures integrated over this time window is shown in Fig. 1. The overall intensity first increases with rising temperature up to about 40 K and then starts to decrease. At low temperatures, different vibronic subbands are clearly resolved, evolving into a broad structureless band around $\langle E_{\mathrm{PL}}\rangle = 1.73$ eV at temperatures higher than $T=200$ K.

III. MODELING OF THE TIME-RESOLVED PL SPECTRA

In order to model the PL spectra over the whole temperature range, we have introduced six components with different decay times and line shapes.

For the four most prominent PL channels, the line shapes were constructed from a series of subbands with a spacing of about 0.16 eV assigned to different harmonics of an effective molecular vibration. For each PL channel, the radiative recombination starts from a specific relaxed excited state, deformed with respect to the equilibrium geometry in the electronic ground state. Therefore, after the radiative recombination to the electronic ground state, different vibronic levels of this effective mode can be reached, and the transition probabilities expressed by the Franck-Condon factors are expected to follow a Poisson progression. The argument g^2 of this Poisson distribution can be related to the reorganization energy λ of each PL channel according to $g^2 \approx \lambda/\hbar\omega_{\mathrm{eff}}$. From the calculation of the configuration coordinate diagrams of the three PL bands assigned to different deformed dimers,[17] we expect in each of these cases $\lambda < \hbar\omega_{\mathrm{eff}}$ or $g^2 < 1$ for the argument of the corresponding Poisson distribution. In the following, g^2 for each PL channel is treated as a phenomenological fitting parameter, and the resulting values are of the order of $g^2 \approx 0.5$; cf. Table I.

From the dominating radiative recombination channel at low temperature[13] and model calculations,[16,18] we found strong evidence for recombination from the dispersion minimum of the Frenkel excitons, with an average energy of $\langle E_{\mathrm{PL}}\rangle = 1.78$ eV resulting from a large subband at 1.83 eV and smaller subbands for the higher harmonics at 1.67 eV and 1.51 eV. At low temperature, this PL channel decays within a radiative lifetime of 13 ns,[13] but at room temperature, its intensity is strongly reduced due to a large nonradiative deexcitation rate.

Furthermore, two PL channels with smaller intensities produce fast-decaying satellites at high energy, but each of them contributes only in a certain temperature range. At low temperatures, this satellite band occurs around 1.95 eV, and for $T > 150$ K, it is quenched due to nonradiative decay. Instead, a different PL band near 2.05 eV develops. Based on the Frenkel exciton model, this high-energy feature can be assigned to a relaxed excited monomer, with an energy corresponding to the average of the lowest Frenkel exciton branch $E_{00}(\mathbf{k})$ over the Brillouin zone.[16] Alternatively, the

TABLE I. Parameters of the PL model including three types of self-trapped excitons, with the energetic positions in the limit $T \to 0$ K. For each vibronic subband, the position, full width at half maximum (FWHM), and relative area a_j are given according to Eq. (3). For simplicity, the area a_2 of the second harmonics is assumed to follow a Poisson progression of argument $g^2 = a_1/a_0$, i.e., $a_2/a_0 = g^4/2$. For the low-energy CT exciton and the excimer, the second harmonics would be hidden under the large broadening of the first sideband, so that we made no attempt to assign its area.

Component	$\langle E_{\mathrm{PL}}\rangle$ (eV)	Blueshift (meV/K)	Subband (meV)	FWHM (meV)	Area	Subband (meV)	FWHM (meV)	Area	Subband (meV)	FWHM (meV)	Area
CT	1.78	3.9×10^{-2}	1845	94	1	1687	105	0.53	1529	165	0.14
CT	1.67	6.2×10^{-2}	1705	128	1	1551	160	0.40			
Excimer	1.72	≈ 0	1757	140	1	1612	160	0.46			

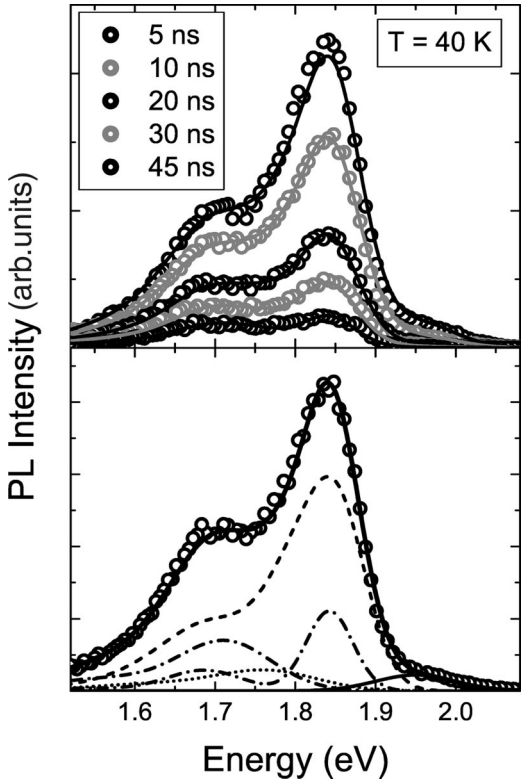

FIG. 2. Upper: evolution of the α-PTCDA PL spectra measured at $T=40$ K as a function of delay after the excitation pulse (circles). Each trace for a given delay t corresponds to a time integration over an interval of 2.5 ns for a representative sample of delay times $t=5$, 10, 20, 30, and 45 ns. The solid lines represent the calculated curves based on our model for the time-dependent PL. Lower: decomposition of the PL spectra integrated between delays of -5 ns and 45 ns (circles) into the different recombination channels, with the Frenkel component (dashed line), the excimer band (dotted line), the two CT channels (dash-dotted line), and the sum of all components (solid line), including a high-energy band at 1.95 eV (solid line).

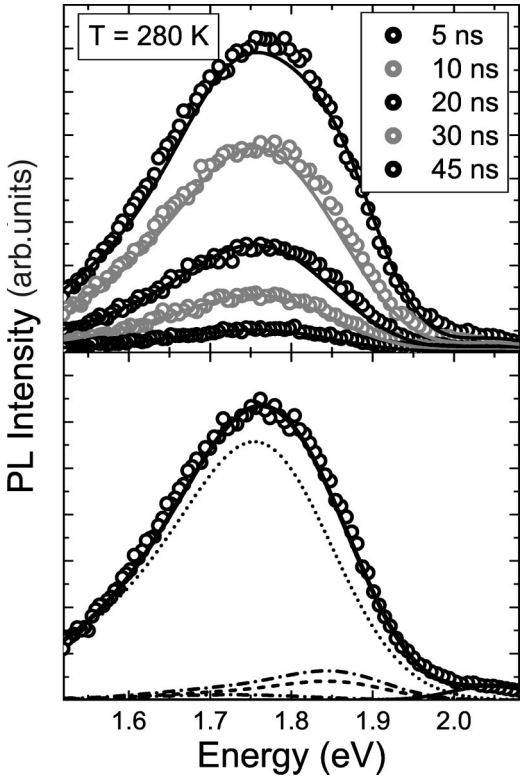

FIG. 3. As Fig. 2, but for $T=280$ K. At this temperature, the high-energy band included in the sum of all components is located at 2.05 eV.

high activation barrier for nonradiative decay of the Frenkel exciton PL could be an indication that the high-energy satellite results from the second-lowest vibronic level of the Frenkel exciton dispersion; cf. Sec. V for further details.

In the numerical data analysis, it cannot be proved or disproved whether the small high-energy satellites also have a vibronic sideband at lower energy, because these features would be in the same energetic region as much larger PL bands arising from different recombination mechanisms. Therefore, the low-temperature satellite at 1.95 eV and the high-temperature band at 2.05 eV were modeled each as a single Gaussian PL band, and in the latter case, details of the shape could be influenced by the use of a cutoff filter at 2.10 eV.

In Figs. 2 and 3, we show two typical decompositions of the PL into the four most prominent channels and the two kinds of high-energy satellites. The PL spectra at $T=40$ K shown in Fig. 2 are dominated by a PL band decaying within 12 ns assigned to Frenkel excitons,[16,18] whereas two slower recombination channels decaying within about 40 and 50 ns, respectively, are assigned to CT transitions between two oppositely charged molecules in different deformed dimer geometries.[17] The fourth channel, assigned to an excimer in a stack geometry,[17] decays 2 times faster than the PL arising from the ionic pairs. The high-energy satellite around 1.95 eV decays within 3 ns, and the intensity of the low-energy CT band rises for the first few nanoseconds with a similar time constant, an indication that the decay of the former could possibly feed the precursor state of the latter.

For the high-temperature spectra at $T=280$ K shown in Fig. 3, the PL due to Frenkel excitons and recombination between ionic pairs is strongly quenched, and instead the excimer band has become the most prominent feature, decaying within about 20 ns. The high-energy satellite at 2.05 eV decays within about 3 ns, with a large uncertainty of the decay rate due to the very low intensity with respect to the other PL channels.

For the four major PL channels, the quantitative details of their model line shapes and the temperature dependence of their decay times and PL intensities are discussed in the next two sections.

IV. INTERPOLATION BETWEEN DIFFERENT TEMPERATURES

The assignment of the same PL channels at different temperatures requires a smooth interpolation of the temperature dependence of the model line shapes. With rising temperature, the broadenings of the vibronic sublevels of the differ-

ent PL channels tend to increase. These broadenings are related to internal A_g modes far below the effective mode, and both for neutral excited molecules and charged molecules, the expected elongations of these modes can be quantified.[19] Therefore, changes of the thermal broadening with temperature can be compared with the contributions expected from the elongations of the low-frequency modes.

A. Frenkel exciton PL band

In the following, the modeling of the Frenkel exciton PL band will be based on its line shape at low temperatures.[13] More specifically, due to the fact that the Frenkel exciton PL dominates over the other PL channels at low temperature, the pronounced asymmetry of its largest vibronic subband is of crucial importance for the correct assignment of the slower and less intense PL channels.

With rising temperature, the peak positions of the Frenkel exciton PL shift to the blue with a slope of 4.8×10^{-2} meV/K. This blueshift can be related to a thermal population of Frenkel excitons around the indirect minimum of their dispersion. The small deviation of the slope from $k_B/2 = 4.3 \times 10^{-2}$ meV/K results from the nonparabolicity of the excitonic band structure.[18] It can be shown that the low-frequency modes with $\hbar\omega \ll \hbar\omega_{\text{eff}} \approx 0.16$ eV are responsible for the broadening and asymmetry of the strongest vibrational subband in the PL spectra at low temperature[16,18] and for the broadening of the subbands of the optical absorption spectra.[15,19,20] At finite temperature, the broadening increases due to the population of higher vibronic levels of the low-frequency modes in the excited-state potential. For a single harmonic oscillator with reorganization energy $\lambda = g^2\hbar\omega$, the temperature dependence of the PL broadening is given by

$$\sigma^2 = (\Delta E)^2 = g^2(\hbar\omega)^2[1 + 2n_{\text{th}}(\hbar\omega, k_B T)] = g^2(\hbar\omega)^2 \coth\left(\frac{\hbar\omega}{2k_B T}\right), \tag{1}$$

where $n_{\text{th}}(\hbar\omega, k_B T)$ is the average number of excited quanta according to Bose-Einstein statistics. From a previous analysis of the Raman activity and the broadening of the absorption spectra,[15] the temperature dependence related to the internal A_g modes at 537 and 624 cm^{-1} with $\hbar\omega \gg k_B T$ can be ignored, while the pronounced temperature dependence due to the lowest internal breathing mode at 233 cm^{-1} and to the external phonons has to be taken into account. This analysis of the broadening of the linear optical spectra can be applied to the corresponding Frenkel exciton PL band. Replacing the broadening related to the modes at 537 and 624 cm^{-1} by a temperature-independent term σ_{0j} and the six phonon modes by an effective external mode, the temperature dependence of the Gaussian broadening of the vibrational subband j can be expressed as

$$\sigma_j^2 = \sigma_{0j}^2 + g_{\text{int}}^2(\hbar\omega_{\text{int}})^2 \coth\left(\frac{\hbar\omega_{\text{int}}}{2k_B T}\right) + g_{\text{ext}}^2(\hbar\omega_{\text{ext}})^2 \coth\left(\frac{\hbar\omega_{\text{ext}}}{2k_B T}\right), \tag{2}$$

where the second term is related to the broadening due to the internal A_g mode at $\hbar\omega_{\text{int}} = 233$ cm^{-1} with $g_{\text{int}}^2 = 0.29$,[19] and the third term results from an effective external vibrational mode at $\hbar\omega_{\text{ext}} = 50$ cm^{-1} with $g_{\text{ext}}^2 = 7.5$ summarizing the elongations of the six external phonon modes determined from resonant Raman measurements.[15,21] In the PL analysis at higher temperatures, we assume a line shape for the Frenkel exciton based on the experimental contribution at low temperature with its asymmetric vibronic subbands,[13] but we include an increase of the second moment of each subband compatible with Eq. (2).

B. PL bands resulting from localized self-trapped excitons

Each of the PL bands related to the self-trapped excitons is modeled as a sum of exponentially decaying normalized Gaussians with positions ω_j, broadenings σ_j, and areas a_j:

$$I_{\text{PL}}(\hbar\omega, t) = \frac{\omega^3}{\tau} \exp\left(-\frac{t}{\tau}\right) \sum_j \frac{a_j}{\sigma_j \sqrt{2\pi}} \exp\left[-\frac{1}{2}\left(\frac{\omega - \omega_j}{\sigma_j}\right)^2\right], \tag{3}$$

where the multiplicative factor ω^3 is related to the density of states of the emitted photons.[22] The spacing between subsequent positions ω_j corresponds to the effective vibrational mode ω_{eff} for this PL channel. The ratio of the areas a_j of the vibronic subbands are described according to a Poisson distribution $P_j(g^2)$,

$$a_j \propto P_j(g^2) = \frac{g^{2j}}{j!} e^{-g^2}, \tag{4}$$

where the argument g^2 is the vibronic coupling constant. Similar to the Frenkel component, the positions of the vibronic subbands were assumed to have a linear temperature dependence. The broadenings are expressed as

$$\sigma_j^2(T) = \sigma_j(T=0) \coth\left(\frac{\hbar\Omega}{2k_B T}\right), \tag{5}$$

with an effective low-frequency mode $\hbar\Omega \ll \hbar\omega_{\text{eff}}$. As all STE PL bands arise from different relaxed excited dimer states, it is not possible to relate their broadenings to linear absorption or to the Raman activity of the various internal and external vibrations, so that only a comparison with the calculation of the corresponding configuration coordinate diagrams[17] can give some indication. Therefore, the broadenings $\sigma_j(T=0)$ and the energy $\hbar\Omega$ are free fitting parameters allowing one to interpolate the PL line shape between different temperatures, where $\hbar\Omega$ can be interpreted as an effective localized low-frequency vibration coupled to the STE state.[23]

Finally, the parameters used in Eqs. (3)–(5) were optimized simultaneously for all the spectra taken at different delays after the excitation pulse and at different temperatures. The root-mean-square deviations between the simulated curves and the experimental spectra normalized to the total area of the spectra integrated over delay were used as a minimization parameter. The fit quality was better than 1% of the spectral area in the time-integrated data, close to the

range of the signal-to-noise ratio. As an example, the line shapes of the different components are shown in Fig. 2 for $T=40$ K and in Fig. 3 for $T=280$ K.

The peak positions at $T=0$ K, the elongation parameters g^2, and the full width at half maximum at $T=0$ K related to the broadening parameters σ_j by $\mathrm{FWHM}_j=\sqrt{8ln2}\hbar\sigma_j$ are summarized in Table I for the two CT exciton bands and the excimer. The resulting blueshifts of the peak positions are 3.9×10^{-2} meV/K and 6.2×10^{-2} meV/K for the high- and low-energy CT excitons, respectively, whereas the position of the excimer band is temperature independent within the numerical error margins. The localized vibrational mode $\hbar\Omega$ determining the temperature dependence of the broadening is about 30 meV for the high-energy CT exciton, probably coinciding with the lowest internal A_g mode. On the other hand, for the low-energy CT exciton and the excimer, the overall larger broadenings seem to be temperature independent in the measured temperature range.

Even though our fitting procedure is already quite involved, there are still some small deviations between the simulated spectra and the measured data at early delay times; cf. Figs. 2 and 3. One possible reason is not completely thermalized exciton distributions in this time regime. A second more likely explanation for these deviations are low-energy tails of the fast decaying pre-peak at 1.95 eV at low temperature and at 2.05 eV at high temperature, but we did not attempt any quantitative assignment of these small structures at short delay times after the optical excitation.

V. EXCITON KINETICS AS A FUNCTION OF TEMPERATURE

After a consistent fit of the various PL line shapes at different temperatures, the temperature dependence of the corresponding decay times and PL intensities can be analyzed; cf. Fig. 4. The decay time τ of each of the PL channels is modeled as a superposition of a radiative recombination rate and activated nonradiative decay:[24]

$$\frac{1}{\tau}=\gamma=\gamma_{\mathrm{rad}}+\gamma_{\mathrm{nrad}}\exp\left[\frac{-\Delta_{\mathrm{act}}}{k_BT}\right], \tag{6}$$

where $\gamma_{\mathrm{rad}}=\tau_{\mathrm{rad}}^{-1}$ is the inverse of the radiative lifetime, γ_{nrad} a nonradiative recombination rate, and Δ_{act} the corresponding activation barrier; cf. Fig. 4 and Table II. For simplicity the lifetime obtained for the lowest temperature is interpreted as the radiative lifetime of each PL band, but temperature-independent nonradiative decay channels without activation barrier might contribute even in this temperature regime, especially for the slowest recombination channels.

The temperature-dependent lifetimes of the different PL bands are calculated using $\tau_{\mathrm{rad}}=(13\pm2)$ ns for the Frenkel exciton, (42 ± 6) ns for the high-energy CT band around $\langle E_{\mathrm{PL}}\rangle=1.78$ eV, (53 ± 6) ns for the low-energy CT band around $\langle E_{\mathrm{PL}}\rangle=1.67$ eV, and (25 ± 3) ns for the PL arising from the stacked excimer around $\langle E_{\mathrm{PL}}\rangle=1.72$ eV. The ratio between the radiative decay rates of the low-energy CT exciton and the excimer PL band is in agreement with the ratio of the oscillator strengths calculated for the corresponding dimer geometries.[17]

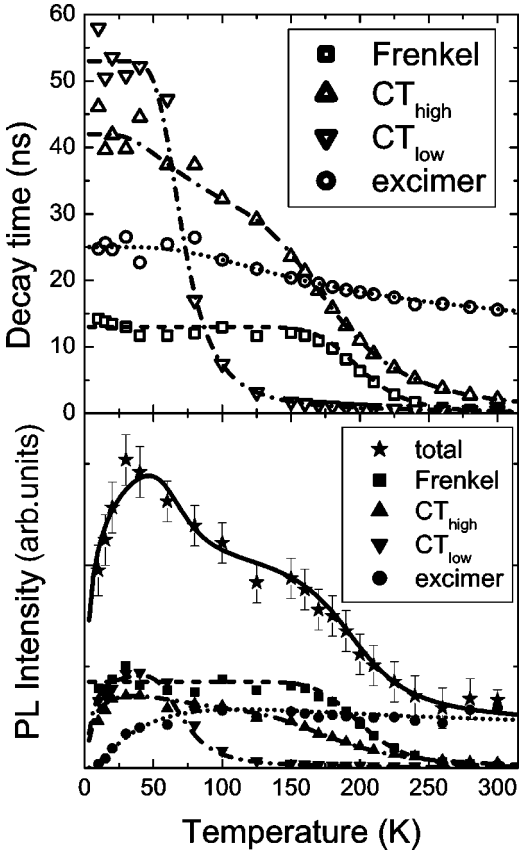

FIG. 4. Top: lifetimes of the different PL bands, where the model curves according to Eq. (6) are calculated with $\tau_{\mathrm{rad}}=13$ ns for the Frenkel excitons, 42 ns for the high-energy CT band around $\langle E_{\mathrm{PL}}\rangle=1.78$ eV, 53 ns for the low-energy CT band around $\langle E_{\mathrm{PL}}\rangle=1.67$ eV, and 25 ns for the PL arising from the stacked excimer. Bottom: temperature-dependent intensities of the different PL bands, with model curves based on the efficiencies η and densities n according to Eqs. (6)–(8) and formation barriers of $E_{\mathrm{form}}=0.3$ meV for the high- and low-energy CT bands and 2.7 meV for the excimer. In the lower panel, the intensities are given in units of $\int dtI(\omega,t)/\omega^3$, excluding the prefactor ω^3 related to the density of states of the emitted photons; cf. Eq. (3).

Concerning the PL bands assigned to the Frenkel exciton, excimer, and low-energy CT state, the resulting deexcitation barriers are $\Delta_{\mathrm{act}}=190$ meV, 26 meV, and 40 meV, respectively. Only in the case of the high-energy CT band can two nonradiative deexcitation barriers of $\Delta_{\mathrm{act}}=12$ meV and 109 meV be distinguished.

The high activation energy of $\Delta_{\mathrm{act}}=190$ meV for nonradiative decay of the Frenkel exciton is close to the energetic spacing between the two lowest dispersion branches at the surface of the Brillouin zone, $E_{01}(\mathbf{k})-E_{00}(\mathbf{k})=0.21$ eV,[16] so that the high nonradiative deexcitation rate $\gamma_{\mathrm{nrad}}=4$/ps could be due to the large density of states on the second-lowest dispersion branch. Furthermore, the high-energy satellite around 2.05 eV develops precisely in the temperature range where the PL due to Frenkel excitons is quenched. Therefore, it is tempting to assign this satellite to recombination from the minimum of the dispersion branch $E_{01}(\mathbf{k})$.

Even though the low-energy CT state is energetically be-

TABLE II. Radiative and nonradiative components of the decay of the various PL channels according to Eq. (6), given in terms of the corresponding lifetimes $\tau = 1/\gamma$. The barriers for activated nonradiative decay are denoted as Δ_{act} and the barriers for the formation of the emissive state as Δ_{form}; cf. Eq. (8).

Component	τ_{rad} (ns)	Δ_{act} (meV)	$1/\gamma_{nrad}$ (ns)	Δ_{act} (meV)	$1/\gamma_{nrad}$ (ns)	Δ_{form} (meV)
Frenkel	13 ± 2	190	0.00025			–
CT (1.78 eV)	42 ± 6	12	35	109	0.03	0.3
CT (1.67 eV)	53 ± 6	40	0.08			0.3
Excimer (1.72 eV)	25 ± 3	26	15.6			2.7

low all other relaxed excited states resulting in radiative recombination, its large nonradiative decay rate $\gamma_{nrad} = 12.5$/ns results in an effective nonradiative quenching already below $T = 100$ K; cf. Fig. 4 and Table II.

The PL efficiency of the different PL channels can be expressed as[24]

$$\eta = \frac{\gamma_{rad}}{\gamma}, \tag{7}$$

so that the temperature dependence of the PL decay rates in Eq. (6) results in radiative efficiencies of $\eta = 1$ at low temperatures. However, this radiative efficiency is defined with respect to the relaxed excited state, resulting in the corresponding PL band, so that the probability to convert the optically created excitons into the corresponding emissive state is excluded from the analysis.

All the STE PL channels involve an energetic barrier Δ_{form} for the formation of their precursor state,

$$n(T) = n_0 \exp\left[\frac{-\Delta_{form}}{k_B T}\right], \tag{8}$$

resulting in a suppression of their densities n and the corresponding PL intensities at temperatures below about $T = 50$ K; cf. Fig. 4. These formation barriers are $\Delta_{form} = 0.3$ meV both for the low- and high-energy CT states and 2.7 meV for the excimer.

The proposed absorption and PL scenario, shown in Fig. 5, can be described as follows. After photon absorption, the Frenkel excitons are created at the Γ point of the Brillouin zone, from where they relax to the minimum of the dispersion at the edge of the Brillouin zone by inelastic scattering mechanisms. From this relaxed Frenkel exciton state they can recombine to the ground state. The temperature dependences of the self-trapped excitons can be assigned to the formation of their precursor states independently of the relaxed Frenkel exciton. From the relaxed STE states, the recombination towards the ground state can proceed via radiative and nonradiative processes.

VI. CONCLUSION

As a conclusion, we have investigated the relaxed excitonic states in α-PTCDA single crystals by means of time-resolved PL measurements in the temperature range from 10 to 300 K. Based on a careful data analysis, we were able to distinguish six different radiative recombination channels. They were assigned to a vertical transition from the indirect minimum of the Frenkel exciton dispersion, three self-trapped dimer states including two CT states and an excimer, and two different high-energy features at low and high temperatures. The Frenkel exciton with a PL maximum at 1.83 eV and a radiative lifetime of $\tau_{rad} = 13$ ns predominates at low temperatures, whereas the excimer with $\langle E_{PL} \rangle = 1.72$ eV and $\tau_{rad} = 25$ ns becomes the most important PL channel at temperatures above $T = 200$ K. The two charge-transfer states with $\langle E_{PL} \rangle = 1.67$ eV and 1.78 eV give the strongest relative contributions between $T = 20$ K and $T = 50$ K, and due to their long radiative decay times of $\tau_{rad} = 53$ ns and 42 ns, the separation of these CT excitons from the intense PL bands with shorter lifetimes requires rather long delay times after the excitation pulse.

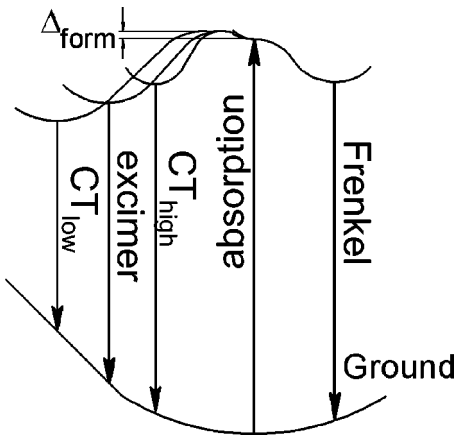

FIG. 5. Schematic configuration coordinate diagram for the Frenkel exciton, the high- and low-energy CT excitons and the excimer state, showing the formation barriers between the exciton created by optical absorption at the Γ point of the Brillouin zone and the self-trapped exciton states. The direction towards the right-hand side (RHS) shows the dispersion of the Frenkel exciton in **k** space (Ref. 16), and the configuration coordinate towards the LHS corresponds to different deformation patterns for each of the localized self-trapped exciton states visualized. For simplicity, the formation barrier visualized is the same for all self-trapped excitons.

At higher temperatures, all PL channels are quenched due to activated nonradiative decay mechanisms, and the excimer PL becomes the most important radiative recombination channel because the influence of nonradiative processes on the recombination rate is much weaker than for the other PL bands. Concerning the temperature dependence of the PL intensities, this model for nonradiative quenching has to be combined with a suppression of the self-trapped excitons at low temperatures due to different energetic barriers for their formation.

ACKNOWLEDGMENTS

The authors gratefully acknowledge the DFG-funded Graduiertenkolleg *Dünne Schichten und nichtkristalline Materialien* at the Technical University of Chemnitz and the EU-funded Human Potential Research Training Network DIODE (Contract No. HPRN-CT-1999-00164) for financial support.

*Present address: Abt. Biophysik, Universität Ulm, D-89069 Ulm, Germany.

†Corresponding author. Electronic address: scholz@physik.tu-chemnitz.de

[1] S.R. Forrest, Chem. Rev. (Washington, D.C.) **97**, 1793 (1997).

[2] A. Djurišić, T. Fritz, and K. Leo, Opt. Commun. **183**, 123 (2000).

[3] I. Vragović, R. Scholz, and M. Schreiber, Europhys. Lett. **57**, 288 (2002).

[4] G. Mazur, P. Petelenz, and M. Slawik, J. Chem. Phys. **118**, 1423 (2003); G. Mazur, Ph.D. thesis, Jagiellonian University, Kraków, 2001.

[5] M. Hoffmann and Z.G. Soos, Phys. Rev. B **66**, 024305 (2002).

[6] F. Stienkemeier and A.F. Vilesov, J. Chem. Phys. **115**, 10 119 (2001); M. Wewer and F. Stienkemeier, Phys. Rev. B **67**, 125201 (2003).

[7] F.F. So and S.R. Forrest, Phys. Rev. Lett. **66**, 2649 (1991).

[8] V. Bulović, P.E. Burrows, S.R. Forrest, J.A. Cronin, and M.E. Thompson, Chem. Phys. **210**, 1 (1996).

[9] A. Nollau, M. Hoffmann, and K. Leo, Thin Solid Films **368**, 130 (2000).

[10] A. Nollau, M. Hoffmann, K. Floreck, T. Fritz, and K. Leo, J. Appl. Phys. **87**, 7802 (2000).

[11] U. Gómez, U.M. Leonhardt, H. Port, and H.C. Wolf, Chem. Phys. Lett. **268**, 1 (1997).

[12] K. Puech, H. Fröb, M. Hoffmann, and K. Leo, Opt. Lett. **21**, 1606 (1996); K. Puech, H. Fröb, and K. Leo, J. Lumin. **72-74**, 524 (1997).

[13] A.Yu. Kobitski, R. Scholz, I. Vragović, H.P. Wagner, and D.R.T. Zahn, Phys. Rev. B **66**, 153204 (2002).

[14] A. Yu. Kobitski, G. Salvan, H.P. Wagner, and D.R.T. Zahn, Appl. Surf. Sci. **179**, 209 (2001).

[15] R. Scholz, I. Vragović, A. Yu. Kobitski, G. Salvan, T.U. Kampen, M. Schreiber, and D.R.T. Zahn, in *Organic Nanostructures: Science and Applications, Proceedings of the International School of Physics "Enrico Fermi," Course CXLIX*, edited by V.M. Agranovich and G.C. La Rocca (IOS, Amsterdam, 2002), pp. 379–402.

[16] R. Scholz, I. Vragović, A.Yu. Kobitski, M. Schreiber, H.P. Wagner, and D.R.T. Zahn, Phys. Status Solidi B **234**, 403 (2002).

[17] R. Scholz, A. Yu. Kobitski, I. Vragović, T.U. Kampen, D.R.T. Zahn, and H.P. Wagner, in *Physics of Semiconductors 2002, Proceedings of the 26th International Conference on the Physics of Semiconductors, Edinburgh, 29 July–2 August 2002*, Institute of Physics Conf. Ser. 171, edited by A. R. Long and J. H. Davies (Institute of Physics, Bristol, 2002), p. 266.

[18] I. Vragović and R. Scholz, following paper, Phys. Rev. B **68**, 155202 (2003).

[19] R. Scholz, A.Yu. Kobitski, T.U. Kampen, M. Schreiber, D.R.T. Zahn, G. Jungnickel, M. Elstner, M. Sternberg, and T. Frauenheim, Phys. Rev. B **61**, 13 659 (2000).

[20] K. Gustav, M. Leonhardt, and H. Port, Monatsch. Chem. **128**, 105 (1997).

[21] G. Salvan, D.A. Tenne, A. Das, T.U. Kampen, and D.R.T. Zahn, Org. Electron. **1**, 49 (2000).

[22] R. Loudon, *The Quantum Theory of Light* (Clarendon, Oxford, 1983), Chap. 2.4.

[23] H. Nishimura, T. Yamaoka, K. Mizuno, M. Iemura, and A. Matsui, J. Phys. Soc. Jpn **53**, 3999 (1984).

[24] N.J. Turro, *Modern Molecular Photochemistry* (University Science Book, Mill Valley, CA, 1991), Chap. 5.7.